Acta Materialia 143 (2018) 319–328

Contents lists available at ScienceDirect

Acta Materialia

journal homepage: www.elsevier.com/locate/actamat

Full length article

Droplet spreading on a surface exhibiting solid-liquid interfacial premelting

Yang Yang [a], Brian B. Laird [b, c, *]

[a] State Key Laboratory of Precision Spectroscopy and Physics Department, School of Physical and Material Science, East China Normal University, Shanghai, 200062, China
[b] Department of Chemistry, University of Kansas, Lawrence, KS, 66045, United States
[c] Freiburg Institute for Advanced Studies, Albertstraße 19, 79104, Freiburg, Germany

ARTICLE INFO

Article history:
Received 29 March 2017
Received in revised form
2 October 2017
Accepted 6 October 2017
Available online 12 October 2017

Keywords:
Solid/liquid interfaces
Molecular-dynamics simulation
Wetting
Droplets
Surfaces

ABSTRACT

We study, using molecular-dynamics (MD) simulation, the spreading kinetics and equilibrium shape of liquid Pb droplets on an Al (111) substrate. The Al-Pb solid-liquid interface was found previously [Phys. Rev. Lett, **110**, 096102 (2013)] to exhibit solid-liquid interfacial premelting at temperatures below the Al melting point. Because the Al(111) free surface does not exhibit premelting, the spreading of a Pb droplet is accompanied by a simultaneous surface transition from a faceted to a premelted Al substrate. Here, we examine how the coupling of the droplet spreading to the premelting affects the spreading kinetics and compare the results to two standard limiting mechanisms of droplet spreading: *hydrodynamic spreading*, in which the spreading energy dissipation is dominated by viscous relaxation, and *kinetic spreading*, where interfacial friction dominates. These two mechanisms predict different power-law dependency for the droplet radius versus time. For temperatures where premelting is present (between 875 K and the melting point of aluminum), kinetic spreading is observed at intermediate times. Because Pb droplets only partially wet the surface, the droplet radius at long times relaxes exponentially to the equilibrium droplet shape. Spreading simulations of a faceted system at 625 K [below the Al(111) roughening temperature] show that this system is consistent with a hydrodynamic spreading mechanism. However, when we examine a system at 922.38 K in which premelting is artificially suppressed by introducing harmonic constraints to give surface vibrations consistent with the Al(111) free surface, we observe a kinetic spreading mechanism - as in the premelted system. When premelting is suppressed, the equilibrium contact angle is observed to be significantly larger than when premelting is present even at the same temperatures. Thus, we conclude that the presence of the premelting layer has a significant effect on the thermodynamics Al(111)/Pb solid-liquid interface, but little effect on the mechanism of spreading. We also observe that the structure of the droplet contact line in the presence of the premelting layer is described by two contact angles (instead of the usual one) due to the presence of the additional premelting layer, and resembles structures seen in reactive wetting systems.

1. Introduction

The kinetics of wetting and spreading of a fluid on a solid substrate has been the subject of considerable scientific interest due to its significance in fundamental science and technology [1–4]. This interest has, in recent years, resulted in a number of experimental [5–11], theoretical [12–14], and computational studies [14–18] for a diverse array of systems.

For the relatively simple case of nonreactive spreading in which a droplet spreads without chemical reaction/dissolution (reactive wetting) or surface phase transitions, the spreading kinetics have been successfully described by universal scaling laws for the time evolution of the droplet profile. These scaling laws have been validated in laboratory and numerical experiments [1,12,19–36]. The dynamics of droplet spreading is determined through a non-equilibrium statistical mechanical approach in which the driving force (determined by the gradient of the droplet free energy with respect to droplet shape) is balanced against the rate of energy

* Corresponding author. Department of Chemistry, University of Kansas, Lawrence, KS, 66045, United States.
E-mail address: blaird@ku.edu (B.B. Laird).

https://doi.org/10.1016/j.actamat.2017.10.018
1359-6454/

dissipation. The scaling laws for droplet spreading are then derived by considering one of two limiting cases: a *hydrodynamic* limit in which the free energy dissipation is assumed to be due only to viscous flow in the droplet and a *kinetic* limit in which interfacial friction is the dominant mode of energy dissipation.

In the hydrodynamic limit, in which the interface friction coefficient (ζ_0) is assumed to be negligible relative to the contribution of the viscosity (η) in determining the dissipation of energy, the time evolution of the radius of a spherical cap droplet $R_{SC}(t)$ and the droplet contact angle, $\theta_{SC}(t)$ can be shown to scale as follows [20].

$$R_{\mathrm{sph,h}}(t) = C_{R,\mathrm{h}} t^{1/10} \tag{1}$$

$$\theta_{\mathrm{sph,h}}(t) = C_{\theta,\mathrm{h}} t^{-3/10} \tag{2}$$

The subscript "h" denotes the hydrodynamic limit. In the kinetic limit [19] (denoted by subscript "k"), where the dominant mode of energy dissipation is assumed to arise from the frictional interaction between the droplet and the substrate and the contribution from the droplet viscosity is neglected, the scaling laws for the droplet radius and contact angle are predicted to be

$$R_{\mathrm{sph,k}}(t) = C_{R,k} t^{1/7} \tag{3}$$

$$\theta_{\mathrm{sph,k}}(t) = C_{\theta,\mathrm{k}} t^{-3/7} \tag{4}$$

Based on detailed analysis of the mechanical dissipation mechanisms of a spreading droplet, de Ruijter et al. [24] predicted that, after an initial linear time regime of length t_1, the droplet spreading will exhibit kinetic spreading, crossing over to a hydrodynamic regime after a time t_2, which is proportional to $(\zeta_0/\eta)^{3/7}$. For a system in which the droplet fluid only partially wets the substrate, the above scaling laws should only apply on intermediate time scales. At long times, the approach to the equilibrium radius, R_e, for both models is predicted to be exponential [24].

$$\Delta R(t) = R(t) - R_e \approx C_e e^{-t/\tau} \tag{5}$$

In the case of reactive wetting, in which the surface composition of the droplet or substrate changes due to chemical reactions or, in the case of mutual miscibility between droplet and substrate, dissolution, the energy dissipation and droplet profile evolution can be quite complicated [37–46]. Even when the droplet and substrate materials are nonreactive and mutually immiscible, surface phase transitions can occur that significantly alter the spreading mechanism and kinetics. For example, recent studies [27,47] have demonstrated novel wetting/spreading behavior in the chemically heterogenous Cu(s)/Pb(l) solid-liquid interfacial system. In this system, a strong anisotropy in the droplet spreading kinetics was observed in molecular-dynamics (MD) simulations between the Cu(111)/Pb(l) and the Cu(100)/Pb(l). It was found that the spreading of the Pb droplet on Cu(111) was considerably faster than on Cu(100). On the (111) surface, spreading of the main Pb droplet was preceded by the rapid spreading of a precursor foot about 2–3 lattice spacings in thickness. The spreading of the precursor foot was found to follow a $R(t) \sim t^{1/2}$ scaling relationship [27], in agreement with previous experimental and theoretical studies [3]. Later examination of the equilibrium (111) and (100) Cu/Pb solid-liquid interfaces [48] showed considerable structural differences between the two interfaces. For the (100) interface, the first solid layer was observed to be a Cu/Pb surface alloy, whereas the (111) interface exhibited a prefreezing layer of crystalline Pb about 2-3 layers in thickness. It is this prefreezing layer that forms the precursor foot seen in the original MD simulations of Webb et al. [27].

In a recent study [49], we have observed in MD simulations the existence of a premelting transition at the chemically heterogeneous Al(s)/Pb(l) solid-liquid interface. The width of the premelting layer diverges logarithmically with the undercooling as the Al melting point is approached. For the case of the Al(111)/Pb(l) interface, the formation of a premelting layer at the solid-liquid interface contrasts with the observed lack of premelting at the free Al(111) surface. This system then provides a good test case to study the effect of surface phase transition on droplet spreading as spreading of Pb droplets at the (111) Al surface would be coupled to the formation of the premelting layer underneath the spreading droplet.

In this paper, atomistic simulations coupled with theoretically-motivated analysis is carried out to study the spreading and wetting behavior of a Pb droplet on the solid Al(111) surface at temperatures below the melting point of Al, where premelting is observed. The spreading kinetics is examined and found to be consistent with different existing theoretical models at different stages of the spreading process. The wetting shapes in terms of the contact angle of the Pb droplet on Al surfaces are measured and a delicate four phase balance detected and discussed. The paper is organized as follows: In Section 2 the MD simulation and analysis methods are described in detail and the main results and discussion are presented in Section 3, followed by a summary in Section 4.

2. Simulation and analysis methods

2.1. Al/Pb and interatomic potential

In this work, we study the wetting and spreading kinetics of Pb liquid metal droplets on Al(111) surfaces for temperatures ranging from just above the melting point of Pb to just below the melting point of Al. For the interaction model used here, the melting points of Pb and Al are 618 K and 922.4 K, respectively. At the higher temperatures, this system exhibits a premelting layer at the Al/Pb solid-liquid interface [49]. Al/Pb is an ideal model alloy for this study with a simple monotectic phase diagram that contains a broad miscibility gap in the liquid phase and shows negligible solubility in the solid state without any intermediate phases. The equilibrium Al/Pb solid-liquid interfaces are well-defined chemically heterogeneous interfaces as the two substances are highly immiscible over the temperature range studied [50], so we are assured that the wetting of the droplet at the surface is nonreactive.

The interatomic potential for Al/Pb used in this paper is the many-body glue-type EAM potential developed by Landa et al. [51]. The melting points for Pb and Al, as well as the liquid-state miscibility gap, are well described by this potential. For this potential, the equilibrium Al(100)/Pb and Al(110)/Pb solid-liquid interfaces have been reported from MD simulations to be rough over the entire Al(s)/Pb(l) temperature range; however, at lower temperatures near the Pb melting point, the (111) interface is faceted, with a roughening transition at $T_r = 826$ K, above which the interface is rough [49,52]. These results are in good agreement, both qualitatively and quantitatively with the results from transition electron microscopy (TEM) experiments on liquid Pb inclusions in solid Al [50]. In the simulations, solid-liquid premelting was observed at higher temperatures, near the melting point of Al. In agreement with standard theories of premelting [53,54], the width of the premelting layer diverges logarithmically with the undercooling, $\Delta T = T_{\mathrm{m}}^{\mathrm{Al}} - T$.

In this study, we have independently examined with MD simulation the structure of a free Al(111), (110) and (100) surfaces modeled with current potential. These simulations show that both the Al(111) and (100) surfaces remain crystalline up to the melting

point of Al with no surface premelting observed. In contrast, the (110) interface exhibits surface premelting. These results are in agreement with previous experimental and simulation studies [55–59], giving us confidence in the quality of the potential. Some details of these simulations can be found in the Supplemental Information [60]. Because we are interested in the effect of the surface premelting transition on the spreading of droplets, we have limited our study of droplet spreading to the Al(111)/Pb(l) solid-liquid interface as it represents a system in which the equilibrium substrate under the droplet exhibits premelting, but that away from the droplet does not.

2.2. Molecular-dynamics (MD) simulation details

For our simulations, we follow the work of Heine et al. [28,47] in that we examine the spreading of a semi-two dimensional hemicylindrical droplet in order to enable us to model larger droplet radii using a much smaller number of atoms than would be necessary for the study of a fully three-dimensional hemispherical droplet. As discussed in Refs. [28,47], the use of a hemicylindrical geometry changes the form of the scaling laws. For a hemicylindrical droplet, the hydrodynamic model predicts that the droplet radius and contact angle scale as

$$R_{\mathrm{cyl,h}}(t) = C_{R,\mathrm{h}} t^{1/7} \tag{6}$$

$$\theta_{\mathrm{cyl,h}}(t) = C_{\theta,\mathrm{h}} t^{-2/7} \tag{7}$$

whereas, for the kinetic model we have [28].

$$R_{\mathrm{cyl,k}}(t) = C_{R,\mathrm{k}} t^{1/5} \tag{8}$$

$$\theta_{\mathrm{cyl,k}}(t) = C_{\theta,\mathrm{k}} t^{-2/5} \tag{9}$$

For our simulations of a Pb droplet on an Al(111) substrate, we use simulation box dimensions ($L_x \times L_y \times L_z$) of approximately 2300 Å × 35 Å × 700 Å, where the z-axis is defined to be normal to the substrate surface - here Al(111). The y-axis is the short direction in this semi two-dimensional system. Periodic boundary conditions (PBC) are applied in x and y direction, but not in the z direction. The simulation cell in the y direction is chosen to be wide enough such that there are no observable size effects on the values of the equilibrium contact angle and radius measurements of the droplets. We found that $L_y > 30$ Å give results within the uncertainty of these measurements.

The droplets each consist of 67,800 to 423,500 atoms depending on the initial radius of the droplet, R_0. The three initial radii studied here are 20 nm, 35 nm and 50 nm, labeled as system A, B and C, respectively. The substrate consists 168,000 Al atoms arranged in 15 lattice layers of Al atoms. To construct a more realistic substrate, the lower 4 layers of Al atoms in the substrate are held rigid throughout the simulation at a fixed lattice constant corresponding to that calculated for the bulk solid at the temperatures studied. The first 11 layers of Al below the free surface layer are free of any constraints, the width of these free layers is considerably larger than the average of the premelting width, to avoid interaction between the premelted layers and the fixed layers below.

To start the droplet simulations, the hemicylindrical Pb droplet is placed above the substrate to form an initial configuration with a contact angle of 90° for the subsequent MD simulation. In order to further reduce the equilibration time, the initial distance between droplet and the substrate is manually adjusted to minimize the potential energy. Fig. 1 shows the initial configuration for system A.

All MD simulations were performed using the program LAMMPS distributed by Sandia National Labs [61]. The simulations of wetting and spreading start from the initial configurations and the equation of motion within a constant particle number (N), volume (V) and temperature (T) ensemble (NVT) using a time step of 1.0 fs. To thermostat the system, we follow Webb et al. and employ a layered thermostat technique [27,40], which is used as a more realistic way to address the high thermal conductivity in metals, and to avoid local heating/cooling that would result from the application of a homogenous Nosé-Hoover thermostat. In our simulations, each system is divided into 1.0 nm thick rectangular slabs parallel to the substrate surface and the atoms within each slab were controlled using an independent Nosé-Hoover thermostat with a thermostat relaxation time of 0.1 ps. To make analysis easier, the center of mass of the Pb droplet is fixed throughout the simulation.

To examine the dependence of droplet spreading, we determine the spreading trajectories for each of three initial radii - 20 nm, 35 nm and 50 nm - at 922.38 K. All of the droplets studied here are large enough to avoid the droplet size dependence of the equilibrium contact angle observed for smaller system sizes. In addition, the 20 nm system (system A) is examined at 5 different temperatures (625 K, 875 K, 900 K, 912 K and 922.38 K) to study the spreading at different premelting layer widths. At 625 K, the interface is faceted with no premelting and the other four temperatures exhibit premelting but with differing premelting layer widths. In addition, we also perform several simulations at 922.38 K in which premelting is artificially suppressed by either fixing the Al atoms at their ideal lattice sites or by harmonically constraining the surface Al atoms. This was done to determine directly the effect of premelting on the wetting/spreading kinetics. Details of these simulations can be found in the Supplemental Information [60].

Each MD simulation begins from the initial configuration with velocities of Pb atoms randomly distributed according to a Maxwell-Boltzmann distribution at the desired temperature. The system is then evolved with layered-NVT MD for 20 ns to collect data. To improve the statistics, we perform ten replica NVT runs starting from the same configuration but with a different set of velocities. Atomic configurations were sampled from the trajectory every 1.0 ps for the analysis of the spreading kinetics and wetting shape.

2.3. Analysis methods

To determine the kinetics of droplet spreading, the time-dependent droplet shape as well as the radius $R(t)$ of the spreading drop front (or the position of the triple junction) were determined from the MD trajectories. At a given time t, the instantaneous coarse-grained Pb droplet shape profile is determined by first dividing the z-axis above the substrate into slab layers of thickness 2.75 Å, which corresponds to the atomic layer spacing for the packing of Pb atoms along the (111) direction of Al crystal. The droplet shape is calculated from the position of the liquid-vapor interface (defined as the equimolar dividing surface). The lateral size of the slab layers is the same as the xy dimensions of the of the simulation box. Within each slab layer, the fine-grained density profile of Pb along x can be well fitted with two hyperbolic tangent functions for calculating its two equimolar dividing surfaces, $x_{e1}(z)$, $x_{e2}(z)$ [23,62]. $R(t)$ is defined as half the distance between two dividing surfaces in the slab layer just above the substrate. To obtain adequate statistics, $R(t)$ is obtained from an average over 10 independent replica runs.

After reaching the equilibrium state, the equilibrium wetting shape of the Pb droplet was determined by first averaging the single particle density $\rho(\mathbf{r})$ over the y-axis to create a 2-D density map over the xz plane, $\langle\rho(\mathbf{r}_{xz})\rangle$, where the average includes all Pb

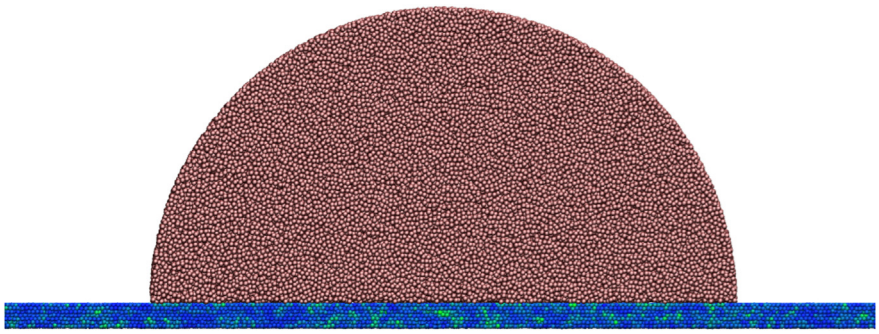

Fig. 1. A side view of initial configuration of wetting system A, with $R_0 = 20$ nm Pb droplet in contact with the (111) surface of Al. Pb atoms are represented in red color and Al atoms are in blue. The droplet spreads along x direction, the hemicylindrical axis is along y direction, and z direction follows the normal of the (111) surface. Note that only a portion of the substrate (in x and z) is shown. (For interpretation of the references to colour in this figure legend, the reader is referred to the web version of this article.)

atoms found in 2000 configurations sampled over 20 ns. The xz plane is partitioned into a 2-D grid (with grid size 0.2 Å × 0.2 Å), and the time-averaged atom number density is calculated in each grid. To calculate the equilibrium shape of the pre-melted Al layer, we first select the liquid Al atoms using a local structural order parameter [63]. All Al atoms with a value of this order parameter below a threshold of 0.2 are defined to be liquid Al atom. Once this is done, the average 2-D (xz) density map for liquid Al was calculated, using the same protocol as for the Pb droplet shape.

The degree of wetting for a droplet on a solid substrate is measured by the equilibrium contact angle at the three-phase junction. The value of the contact angle is the result of the balance of forces at this triple junction. For a system without premelting, this force balance is described by Young's equation for the contact angle, θ:

$$\cos\theta = \frac{\gamma_{sv} - \gamma_{sl}}{\gamma_{lv}} \tag{10}$$

where γ_{sv}, γ_{sl} and γ_{lv} are the solid-vapor, solid-liquid and liquid-vapor interfacial free energies, respectively. In this system, however, the presence of a premelting layer gives us two contact angles. The first, θ_1, is the contact angle between the between Pb liquid-vapor interface and the interface between the Pb liquid and the Al substrate (either solid Al at the lowest temperatures where no premelting is observed, or liquid Al). The second angle, θ_2, is defined only when the premelting layer is present and corresponds to the contact angle between the Pb/Al liquid-liquid interface and Al liquid-solid interface.

The equilibrium contact angle measurements in this work are based on the time-averaged equilibrium coarse grained outlines of the Pb droplet surface (Pb liquid-vapor interface), the Al/Pb liquid-liquid interface and the Al liquid-solid interface. For the equilibrium Pb droplet surface, the time-averaged coarse grained outline was obtained through averaging 2000 instantaneous Pb droplet shape profiles over 2ns after reaching equilibrium, $\langle x^{\mathrm{Pb}}(z)\rangle_{\mathrm{eq}}$. The equilibrium Al/Pb liquid-liquid interface was treated as flat horizon extending along the Al (111) surface - an assumption that was verified from the average 2-D density map of the Pb droplet and the premelted liquid Al. Similarly, the coarse grained outline of the equilibrium Al/Al solid-liquid, $\langle x^{\mathrm{Al}}(z)\rangle_{\mathrm{eq}}$. was determined by calculating the time-averaged equimolar dividing surfaces (here the Al/Al solid-liquid interface) within horizontally coarse-grained slab layers with thickness 2.2 Å.

The contact angles were then calculated straightforwardly by applying linear fittings to the first five data points of $\langle x^{\mathrm{Pb}}(z)\rangle_{\mathrm{eq}}$ and the first three data points of $\langle x^{\mathrm{Al}}(z)\rangle_{\mathrm{eq}}$ closest to the horizontal line (substrate surface), to extract the value of contact angles θ_1 and θ_2 from the fitting slope, respectively. The statistical errors were estimated by averaging 20 samples from 10 independent replica simulations - each containing two independent contact lines. To note here, the data points corresponding to the interfacial intermixing layer were excluded in the linear fittings. In the previous computational work by de Ruijter et al. [23], the contact angle was measured from the extrapolated circle through the outline profiles and the region that influenced by the substrate had been excluded. In this study, the near contact line region (1–2 nm) of the outline profile is strongly influenced by the substrate made of a chemically dissimilar substance, as well by the presence of the interfacial premelting transition. Therefore a linear fitting to the contact line, where the four phases meet each other, is preferred to measure exact contact angles.

3. Results and discussion

3.1. Coupling of droplet spreading with premelting transition

As discussed earlier, the equilibrium Al(111)/Pb(l) interface exhibits premelting near the Al melting point; however, the Al(111) free surface does not. Therefore, as a Pb droplet spreads over an Al(111) surface at these temperatures, the Al premelting layer must form under the droplet as the system approaches equilibrium. To examine this, we show in Fig. 2 simulation snapshots (side view) of the time evolution of the contact line for system A ($R = 20$ nm) at $T = 922.38$ K after 0.01, 0.24, 1.00 ns and 6.00 ns. In this figure, the Al atoms that have been identified by the order parameter described in the previous section as liquid are shaded green to distinguish them from those Al atoms determined to be crystalline (blue) and the liquid Pb atoms (red). This series of snapshots shows that the premelting layer underneath the spreading droplet forms instantaneously as the droplet spreads, indicating that the kinetics of premelting is considerably faster than that of spreading. The width of the premelting layer is also relatively constant with time.

Another view of the coupling of the droplet spreading with the premelting layer is shown in Fig. 3. In this figure, the advancing premelting layer is viewed from above with the Pb atoms removed from the image. As in Fig. 2, the liquid Al atoms, as identified by the order parameter [63] are shown in green with the solid Al atoms in blue. To give a baseline, the panel (a) shows the Al(111) surface in the absence of a lead droplet. Panels (b) through (e) correspond to the four panels of Fig. 2. The voids seen in panel (e) are due to fluctuations in the position of the Al/Pb liquid-liquid interface and the fact that the Pb atoms are not shown. Animations showing the full time evolution of the trajectories as shown in Figs. 2 and 3 are provided in the Supplemental Information [60].

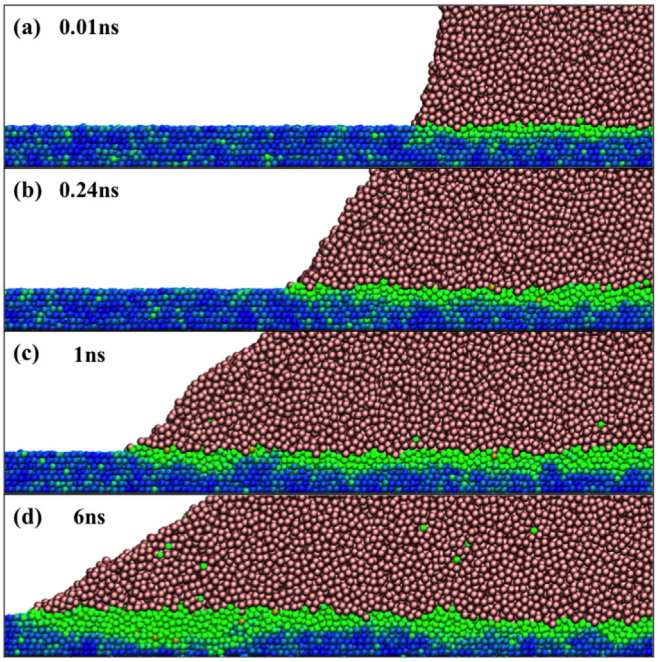

Fig. 2. Snapshots (side view) of the droplet spreading coupled with the premelting transition at several times during Pb droplet evolution at 922.38 K. The Al atoms are color coded as crystalline (blue) or liquid-like (green) according the value of the order parameter discussed in the previous section. The liquid Pb atoms are shown in red. (For interpretation of the references to colour in this figure legend, the reader is referred to the web version of this article.)

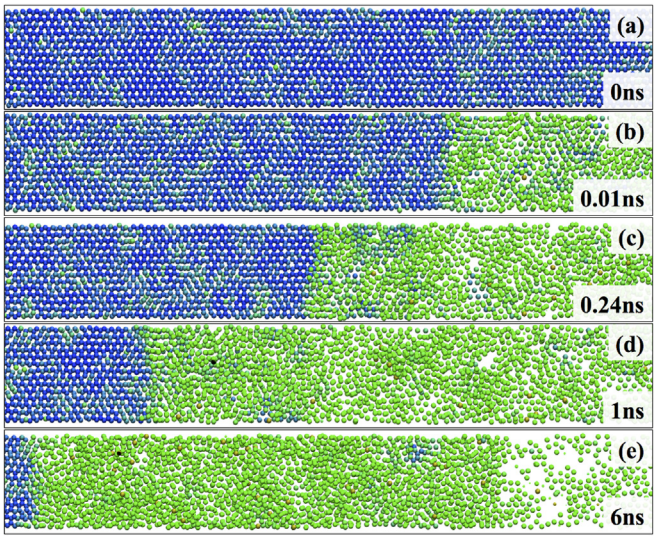

Fig. 3. Top view of the upper two surface layers of Al for the droplet-spreading snapshots shown in Fig. 2. The Pb atoms not shown. The Al atoms are color coded as crystalline (blue) or liquid-like (green) according the value of the order parameter discussed in the previous section. (For interpretation of the references to colour in this figure legend, the reader is referred to the web version of this article.)

3.2. Spreading kinetics

The spreading kinetics is characterized by the time-evolution of the line of contact of the droplet with the underlying substrate. For system A at $T = 922.38$ K, the early-time spreading stage (0–0.2 ns) follows a linear time-dependence of the radius, consistent with theory [24]. - see in Fig. S4 in Supplemental Information [60]. In the left panel of Fig. 4 the contact radius of the spreading droplet as a function of time (beyond 0.2 ns) is plotted on a linear-log scale for system A at $T = 922.38$ K. The red solid line shows the time evolution averaged over the multiple replica simulations, which are shown individually in grey. The averaging is seen to precise enough to distinguish between the different spreading mechanisms. In the time regime (0.2–0.6 ns), $R(t)$ fits well to a power law ($R(t) = C_R t^{n_R}$) with $n_R \approx 1/5$, consistent with that expected for a cylindrical droplet within the kinetic model [28]. See Table 1 for specific values of n_R and C_R, for the fits. In this time regime, the spreading is consistent with a model in which the dominant contribution to energy dissipation is due to the kinetic attachment of the Pb atoms to the Al surface.

The contact radius of the droplet reaches an equilibrium value of about 36 nm at long times ($t > 5$ ns), indicating that Pb(l) only partially wets Al under these conditions. Assuming the radius is constant after 5 ns allows us to estimate of the equilibrium radius, R_{eq}. The right panel of Fig. 4 shows the approach to the equilibrium droplet shape. Here the deviation from the equilibrium radius, $R_{eq} - R(t)$, is plotted in a log-linear plot versus the spreading time. After about 0.6 ns, the approach to equilibrium is shown to be well described by exponential relaxation, that is, $R_{eq} - R(t) = C_e \exp(-t/\tau)$, consistent with theoretical studies of the spreading of partially wetting droplets [24]. Here τ is the lifetime of the exponential decay. No hydrodynamic dissipation regime, that is, $R(t) = C_R t^{1/7}$, was seen in any stage of the spreading evolution. The values for C_e and τ are shown for all interfaces studied in Table 1. From this and the analysis of de Ruijter et al. [24], we can conclude that the crossover time, $t_2 \propto (\zeta_0/\eta)^{3/7}$, is larger than the time of onset of exponential relaxation, leading to no observable hydrodynamic regime.

To determine the temperature dependence of the spreading kinetics we have calculated the time-dependence of the droplet radius at four different temperatures (875 K, 900 K, 912 K and

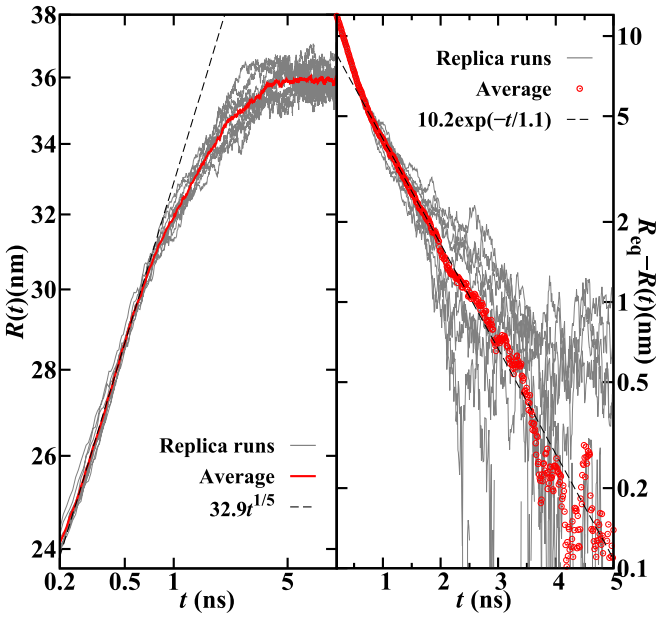

Fig. 4. Left panel: Log-Log plot of $R(t)$ radius of Pb droplet as a function of time for system A at 922.38 K. Right panel: Linear-Log plot of the difference between $R(t)$ and R_e, the equilibrium radius, for the same system as in the left panel. The red lines shows the radius evolution averaged over the ten replica runs (shown individually in grey). The dashed lines (left panel) are fittings to the kinetic model ($R(t) = C_k t^{1/5}$), and to an exponential relaxation model (Eq. (5)) (right panel). (For interpretation of the references to colour in this figure legend, the reader is referred to the web version of this article.)

Table 1
Summary of simulation data: R_0 and T are the initial radius and temperature. The substrate type indicates whether the substrate surface is premelted (PM); harmonically constrained (HC1 and HC2) (see text); rigid (R); or faceted (F), as is the case for the substrate at 625 K. For the intermediate time regime, n_R is the power-law exponent resulting from the fitting, and C_R is the prefactor determined from that fit. (The classification [h] or [k] is used to denote whether the fits are consistent with the hydrodynamic or kinetic models, respectively. For the long-time exponential decay, C_e and τ are the calculated prefactor and decay time, respectively. Equilibrium properties measured from partial wetting simulation: R_{eq}, w, θ_1 and θ_2. Note, the values of w and θ_2 are not applicable for the HC1, HC2, R and F substrates. Error bars represent the 95% confidence intervals on the last digit(s) shown.

R_0 (nm)	T (K)	Substrate	n_R	C_R (nm ns^{-n})	C_e (nm)	τ (ns)	R_{eq} (nm)	w (nm)	θ_1 (°)	θ_2 (°)
50	922.38	PM	0.213(2) ≈ 1/5	64.69(15)[k]	21.8(12)	3.8(2)	90.2(4)	0.98(8)	34.4(4)	10(2)
35	922.38	PM	0.211(2) ≈ 1/5	49.73(9) [k]	14.0(12)	3.0(3)	63.4(5)	0.84(3)	34.4(5)	10(2)
20	922.38	PM	0.202(1) ≈ 1/5	32.90(12)[k]	10.2(9)	1.1(1)	36.2(4)	0.68(3)	33.3(4)	14(2)
20	912	PM	0.201(2) ≈ 1/5	32.79(10)[k]	9.8(9)	1.1(1)	35.1(2)	0.60(1)	38.5(9)	18(3)
20	900	PM	0.200(1) ≈ 1/5	32.50(10)[k]	8.6(6)	1.1(1)	34.8(2)	0.52(2)	39.6(9)	21(4)
20	875	PM	0.197(1) ≈ 1/5	32.01(12)[k]	8.0(7)	1.1(1)	33.6(1)	0.46(1)	40.8(4)	27(5)
20	922.38	HC1	0.198(4) ≈ 1/5	32.42(13) [k]	29.0(8)	0.2(2)	29.8(1)	–	56.9(7)	–
20	922.38	HC2	0.143(2) ≈ 1/7	29.40(8) [h]	13.8(10)	0.3(2)	28.7(1)	–	50.3(4)	–
20	922.38	R	0.149(4) ≈ 1/7	28.50(11)[h]	8.0(8)	0.5(2)	29.0(1)	–	55.2(2)	–
20	625	F	0.144(1) ≈ 1/7	28.71(6) [h]	6.4(9)	0.9(1)	30.4(1)	–	48.1(5)	–

922.38 K) for the same initial radius of 20 nm (system A). These results are shown in Fig. 5. Qualitatively, the results for these four temperatures show very similar behavior, namely, a kinetic dissipation stage (left panel of Fig. 5) followed by exponential relaxation to the equilibrium contact radius (right panel Fig. 5). Quantitatively, the prefactors (coefficients of the fit to $t^{1/5}$) determined for the kinetic dissipation stage are nearly constant with respect to temperature - see Fig. 5 and the data in Table 1. This indicates that the spreading of the droplet in the kinetic phase is unaffected by the width of the premelting layer, which has been shown to diverge logarithmically with the undercooling [49]. The prefactor, C_e, for the exponential relaxation seen at long times, however, does depend have a significant temperature dependence, increasing by about 25% over the range between 875 K and 922.28 K.

We have also examined the effect of initial droplet size (R_0) on the spreading kinetics. Fig. 6 shows $R(t)$ at 922.38 K for systems A, B and C, which have initial radii of 20 nm, 35 nm and 50 nm, respectively. The results are qualitatively similar with a kinetic dissipation stage followed by the long-time exponential relaxation to the equilibrium shape. However, the onset of both the kinetic dissipation and exponential relaxation stages is shifted to later times as the initial droplet size increases. The kinetic and hydrodynamic models for cylindrical geometries predicts that the prefactor, C_R should scale with R_0^n, with $n = 4/5$ and 6/7 for the kinetic and hydrodynamic models, respectively [47]. Analysis of the three sizes studied yields a value of n of about 0.74, which is most consistent with the kinetic model value of $4/5 = 0.8$. Fig. 6 also shows that the long-time exponential relaxation times increase with increasing initial droplet size, thus longer time needed for the droplet to reach equilibrium for larger size droplet, *e.g.* the exponential fittings in Fig. 6 show the larger size droplet has the longer relaxation time. See Table 1 for data.

In the spreading of Pb droplets on the Al(111), the spreading is accompanied by a simultaneous extension of the premelting layer under the droplet as it spreads. To assess the effect of this premelting layer on the speed and mechanism of droplet spreading, we have carried out three additional spreading simulations at 922.38 K using system A. These simulations use the same

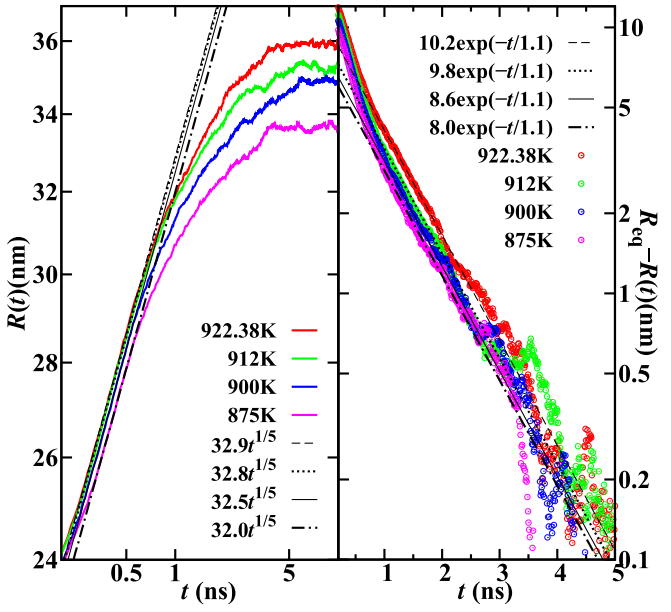

Fig. 5. $R(t)$ of the spreading of the system A droplet for several different temperatures. The presentation is as in Fig. 4, except that only the averaged results, and not those for the individual replicas, are shown.

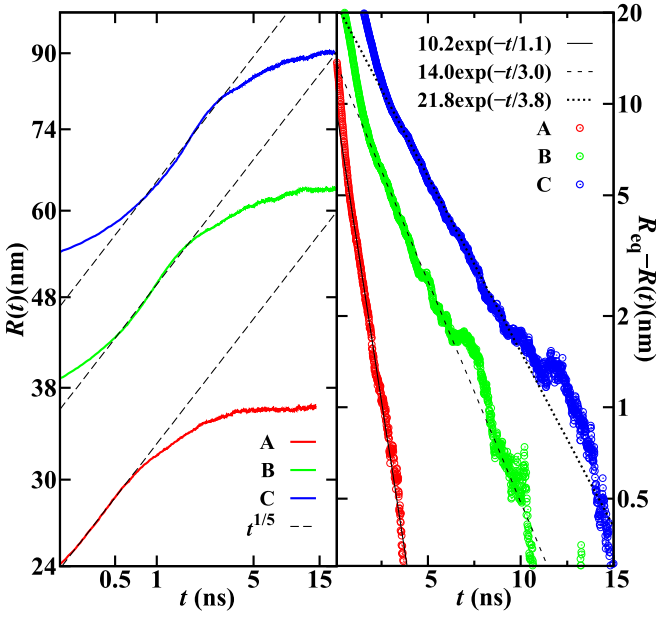

Fig. 6. $R(t)$ of droplet spreading at 922.38 K, for initial droplet radii of 20 nm(red), 35 nm (green) and 50 nm (blue). The presentation is as in Fig. 4, except that only the averaged results, and not those for the individual replicas, are shown. (For interpretation of the references to colour in this figure legend, the reader is referred to the web version of this article.)

parameters and protocol as the previously described system A simulation, except that the substrate atoms are artificially constrained at all times to suppress the premelting. The artificial constraints are added in two ways: (i) all the substrate atoms were held fixed at the original crystal positions - this simulation is labelled "R" for rigid - or (ii) each of the surface atoms were "harmonically constrained", that is, they were tethered to its ideal lattice position with a harmonic force. In one of the harmonically constrained systems, the force constant was tuned to give the same force constant as the an Al(111) free surface at 922.38 K - we label this harmonically constrained simulation "HC1". In the second harmonically constrained simulation (labeled "HC2") [60], the force constant was set to give a surface mean-squared that is one quarter of that of the Al(111) free surface. In addition to the three artificially constrained simulations, we also simulate the spreading/wetting at 625 K, in which premelting is not present. The results for $R(t)$ for these simulations are shown in Fig. 7, together with result of the spreading coupled with interfacial premelting at 922.38 K. These four simulations represent limiting cases for understanding the difference in the spreading mechanism due to thermal surface vibrations, as well as the presence of interfacial premelting. Partial wetting of the droplet on the substrate was found in all simulations.

All of our simulations on the premelted interface follow the kinetic model exclusively without any evidence of a hydrodynamic dissipation regime. In contrast, for both the faceted (625 K) and artificially frozen/rigid (922.38 K) substrates, the time dependence of the droplet radius $R(t)$ (shown for system A in Fig. 7) is observed to scale at intermediate times (0.2 to 0.6~0.8 ns) as t^n, where $n = 0.149(4)$ and 0.144(1), respectively - see Table 1. These power law scalings are consistent with the $t^{1/7}$ scaling law predicted by the hydrodynamic model for hemicylindrical droplet spreading (Eq. (6)) [28].

For the rigid substrate (R) at 922.38 K, the viscosity of the fluid is the same as in the premelted system at this temperature, so the difference in mechanism seen between these two systems implies

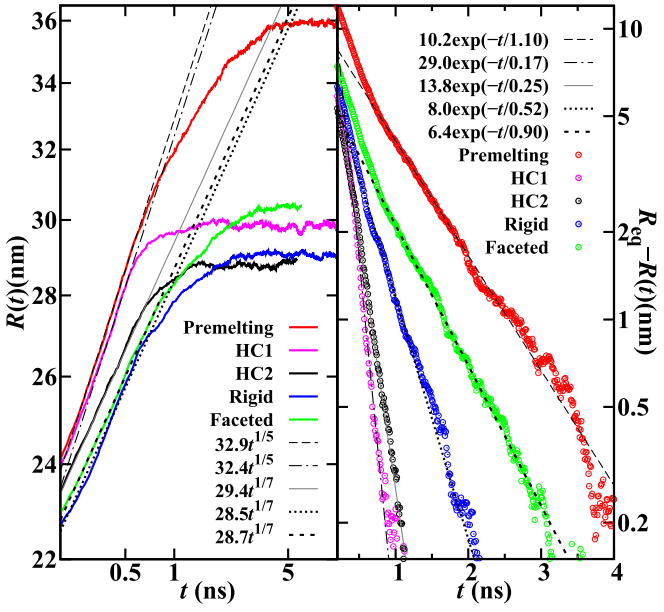

Fig. 7. $R(t)$ of the spreading of Pb droplets (system A) on the rigid substrate (blue) as well as two surface harmonically constrained substrates (magenta and black) at 922.3 K, and on the faceted substrate at 625 K (green). These are compared with the same size droplet at 922.3 K on premelting substrate (red). The dashed and dotted lines were fits according to theoretical predictions. (For interpretation of the references to colour in this figure legend, the reader is referred to the web version of this article.)

that the spreading friction coefficient, ζ_0, of the rigid system must be considerably smaller than that for the premelted one. Therefore, the fact that the full premelted system at 922.38 K follows the kinetic mechanism must either be due to the presence of the premelted layer or to friction caused by solid surface vibrations (which are absent in the rigid simulation). To further resolve this, we examine the results for spreading on the two harmonically constrained systems for which premelting is suppressed, but surface vibrations are present. If the surface vibrations are small as measured by mean-squared displacement (as in the HC2 simulations described above), the spreading is consistent with the $t^{1/7}$ scaling law (hydrodynamic spreading). However, for the larger amplitude vibrations in system HC1, equivalent to those in the free (111) surface at 922.38 K, the spreading follows the $t^{1/5}$ scaling law, in contrast to the spreading on rigid, faceted and HC2 substrates. Therefore, we can conclude that the change in the mechanism of spreading from the faceted system at 625 K (hydrodynamic) to the premelted system at 922.38 K (kinetic) cannot strictly be a consequence of the premelting. In fact, we show in the Supplemental Information [60] that, even for the faceted systems below the roughening transition, the spreading changes from a power law exponent at 625 K of approximately 1/7 (hydrodynamic spreading) to nearly 1/5 (kinetic spreading) just below the roughening transition. Thus, the change from hydrodynamic spreading at low temperatures to kinetic spreading at high temperatures is due to the increased surface friction caused by higher amplitude surface phonons.

Like the premelted surfaces, the faceted and artificially constrained substrates show exponential relaxation at long times, albeit all with faster relaxation times (τ) (See Table 1). The harmonically constrained substrates show the fastest exponential relaxation of all systems studied and the spreading stops rapidly after the kinetic spreading stage. In these systems, Al atoms can only vibrate near the their original lattice sites, they cannot diffuse to other lattice sites. So the final relaxation is limited. Such difference in τ between the spreading on the premelted surface and the harmonically constrained surface suggests that the presence of the premelting layer has significant impact on the final relaxation stage of the droplet spreading.

Existing theoretical models for non-reactive droplet spreading systems also predict time evolution of the instantaneous contact angle (Eq. (7) and (9)) [21–23,28]; however, this is considerably complicated in our current system by the presence of the premelting layer, which leads to two contact angles (see the next section). Because of this and the thermodynamic fluctuations of the liquid-liquid Pb–Al interface, we were unable to get data for $\theta(t)$ of sufficient statistical quality to compare to the theoretical predictions.

3.3. Equilibrium droplet geometry

For a fluid that only partially wets a given substrate, the equilibrium geometry of a droplet is generally described in terms of the equilibrium contact angle, θ, between the equilibrium droplet surface and the plane formed by the substrate. The value of this contact angle is determined by the condition that horizontal forces at the three-phase contact line are in balance, as determined by Young's equation (Eq. (10)). Note that in some cases that the substrate is soft or elastic deformable, the balance for the vertical component of the force is associated with the elastic deformation of the substrate, in which Young's equation is not applicable [13,64,65].

In our current system, the presence of the surface premelting layer complicates this picture by adding a fourth phase to the line of contact. The geometry of this equilibrium droplet is shown in Fig. 8,

along with 2-D contour plots of the time-averaged density maps of the liquid Pb droplet and the Al premelting layer. The equilibrium geometry is described here by two contact angles. The first, θ_1 is the angle of contact between the liquid-vapor surface of the Pb droplet and the liquid-liquid interface between the droplet and the underlying Al liquid of the premelting layer. The second angle, θ_2 is formed between this Pb/Al liquid-liquid interface and the solid-liquid interface between the Al premelting layer and the underlying substrate.

As an example, the equilibrium droplet shape at 922.38 K for system A is shown in Fig. 8. The droplet (Pb) liquid-vapor and premelting layer (Al) solid-liquid boundaries are placed at the Gibbs dividing surface determined from the time-average coarse-grained density profiles. The liquid(Pb)/liquid(Al) and solid(Al)/vapor boundaries are determined from the time averaged composition profiles. The contact angles θ_1 and θ_2 are shown explicitly and are determined geometrically from the intersection of the phase boundaries. It is found that Pb droplet has a half lens shape with upper outline profile well approximated by the arc of a perfect circle. The premelted Al liquid phase, while of uniform width w under the middle of the droplet, tapers to a sharp blade-like shape at the two ends of the droplet. The values of the premelted interface width w are recorded in Table 1. The superimposed color-contour plots of the time-averaged density show significant ordering in both Pb liquid near the interface and in the premelted Al liquid, as expected for a fluid near an interface. The calculated θ_1 and θ_2 for each of the interfaces studied are listed in Table 1.

From the data in Table 1, we observe that the width of the premelting layer for system A increases with increasing temperature from 0.46(1) nm at 875 K to 0.68(3) nm at 922.38 K. This is consistent with the results for this system from Ref. [66], which show the premelting width diverging logarithmically with decreasing undercooling, consistent with standard theories of premelting. We also observe significant system size dependence in the premelting width. In Fig. 9, the width of the premelting layer at 922.38 K is plotted as a function of inverse droplet radius, including the value of 1.17(11) nm for the planar interface (infinite radius) reported in Ref. [66]. A linear regression fit shows that the premelting widths for the various size droplets extrapolate linearly to that for the previously reported planar (infinite radius) interface.

The contact angles θ_1 and θ_2 for system A are also seen in Table 1 to have significant temperature dependence, corresponding to the temperature dependence of the interfacial free energies for the surfaces in contact. Except for the very smallest droplet (system A, 20 nm), the contact angles are not dependent on system size, indicating that the droplet contact geometry is converged for droplet radii above 35 nm. From these results, only the premelting width is seen to have significant system size dependence.

From Table 1, the contact angles, θ_1, for systems without a premelting layer (that at 625 K with a faceted substrate, and the three simulations at 922.38 K in which premelting was artificially suppressed, are significantly larger) than those in which a premelting layer is observed. By considering Young's equation and the assuming that the liquid-vapor and solid-vapor interfacial free energies are the same with or without a premelting layer, these results indicate the presence of the premelting layer lowers the total solid-liquid interfacial free energy significantly from that for the nonpremelted interface, as expected, given the existence of the premelting layer in the first place. Thus, a major conclusion of this work is that the presence of the premelting layer significantly affects the thermodynamics of droplet spreading, but has little effect on the spreading mechanism.

4. Summary

Using molecular-dynamics (MD) simulation, we have investigated the time-evolution and equilibrium wetting shape for the spreading liquid Pb droplet on an Al(111) substrate over a range of temperatures between the melting points of Al and Pb. This system was chosen because earlier work [49] has shown that this interface

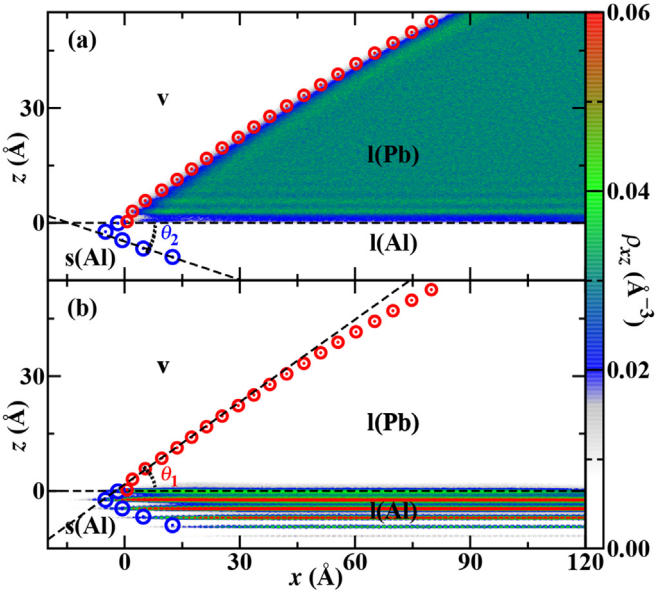

Fig. 8. Equilibrium shape of Pb wetting droplet in the presence of a premelted Al substrate. The corresponding contact angles, θ_1 and θ_2, are labeled. The red and blue open symbols represent the positions Gibbs dividing surfaces of the droplet liquid/vapor and premelting layer liquid/solid interfaces, respectively, as calculated from the time-averaged coarse grained density profiles. Super-imposed on these plots are color-contour plots of the time-averaged density map for (a) the liquid Pb droplet and (b) the premelted Al layer. (For interpretation of the references to colour in this figure legend, the reader is referred to the web version of this article.)

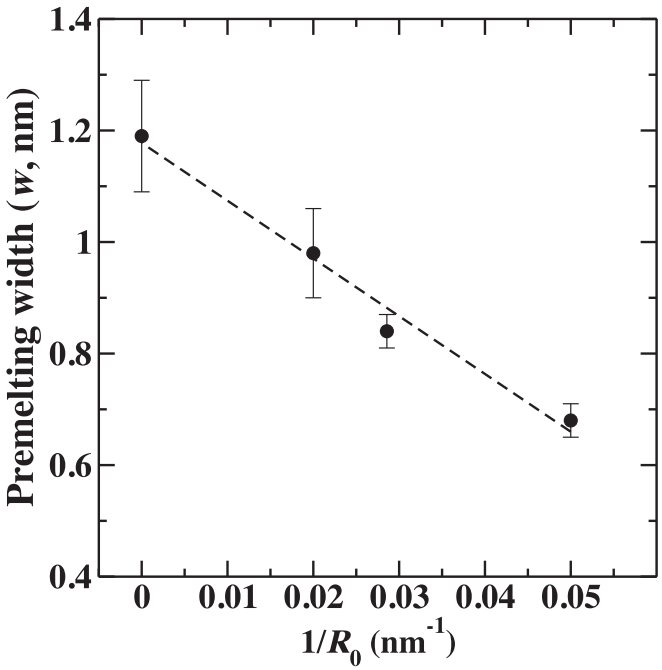

Fig. 9. Width of premelting layer at 922.38 K as a function of inverse droplet radius. Note, the first data point in the figure ($1/R_0 = 0$) was taken from Ref. [49] and was not included in the linear fitting (dashed line).

exhibits solid-liquid interfacial premelting at temperatures below the melting point of Al. However, the Al(111)/vapor interface does not exhibit premelting, so the spreading of a Pb droplet on this surface is coupled to a simultaneous advance of the premelting layer underneath the droplet. Thus, this system provides an excellent opportunity to study the effect of surface phase transition on the kinetics of droplet spreading.

The mechanism of droplet spreading was evaluated from the MD simulations through a careful analysis of the time evolution of the contact radius $R(t)$ for a hemicylindrical droplet. This geometry was chosen, following similar work on Pb droplet spreading on Cu substrates by Heine et al. [47]. Because the system sizes required to obtain statistically meaningful results are much smaller than those required for hemispherical droplets. For droplets that only partially wet a given surface, such the current system understudy, theoretical analysis predicts two possible limiting mechanism for the intermediate time spreading kinetics: *hydrodynamic* spreading, in which the primary energy dissipation channel is viscous relaxation of the fluid droplet, and *kinetic* spreading where energy dissipation is dominated by friction between the droplet and the surface [23,24]. Within the theory, these two mechanisms are predicted to have a power-law dependence of the droplet radius with time, i.e. $R(t) \propto t^n$, with $n = 1/7$ or $1/5$ for the hydrodynamic and kinetic mechanisms, respectively. At long times, the approach to the equilibrium droplet shape is predicted to be of the form of an exponential relaxation. Our analysis shows that for the interfaces studied that exhibit premelting - those above 875 K - the droplet radius obeys a $t^{1/5}$ power law (after an initial linear regime at short times). This is consistent with the kinetic spreading mechanism, implying that interfacial friction is the dominant energy dissipation mode. At long times, all simulations show exponential relaxation to the equilibrium shape - consistent with theories of the spreading of partial wetting droplets.

To analyze the effect of the premelting layer, we have examined four additional Pb/Al(111) systems that do not exhibit premelting - a faceted surface at 625 K, which is below the roughening transition for the Al(111) surface and three systems at 922.38 K (just below the melting point of Al) in which the premelting of the surface has been artificially suppressed in the simulation - either by holding the surface atoms rigid or by the addition of harmonic constraints. The faceted surface at 625 K is shown to be consistent with a hydrodynamic spreading mechanism. Similar behavior is seen in the simulations at 922.38 K in which the surface vibrations are either suppressed or reduced. However, when the surface vibrations are harmonically constrained to have a value consistent with that of the Al(111) free surface at 922.38 K, the spreading is consistent with the kinetic mechanism, like the premelted system at this temperature. Thus, we conclude that the presence of the premelted layer does not significantly alter the spreading mechanism. However, the systems in which premelting is not present show equilibrium contact angles (θ_1) that are significantly larger than those observed when premelting is present. Therefore a major result of this work is that the presence of the premelting layer does not alter the droplet spreading mechanism, but it does have a significant effect on the interfacial thermodynamics.

The shape of the equilibrium droplet was found to be made more complex than usual by the presence of the premelting layer. Instead of the usual three-phase contact line, with a wetting contact angle determined by Young's equation (10), the premelting layer adds a fourth phase to the contact line. Thus, the region around the contact line is defined by two contact angles, θ_1 and θ_2, instead of the usual single wetting contact angles (see Fig. 8). Similar four-phase contact lines have been reported previously for systems undergoing reactive wetting [37–46]. The wetting contact angles as the function of several temperatures and three droplet sizes were measured. Except for the very smallest droplet sizes, the contact angles were not found to have significant size dependences; however, significant temperature dependence of the contact angles was observed due to the temperature dependence of the underlying interfacial free energies.

Through the use of molecular dynamics simulation using realistic potentials, we have demonstrated presence of an accompanying surface phase transformation can have a significant effect on the kinetics and thermodynamics of droplet spreading on a surface. Direct experimental observation of the coupling of the spreading/wetting of droplets with solid-liquid interfacial premelting, or simply the observation of the premelting layer itself, is challenging; however, recent advances in experimental techniques, such as state-of-the-art transmission electron microscopy [67,68] have potential to probe this effect.

Acknowledgements

BBL acknowledges funding from the National Science Foundation [grant No.CHE-0957102]. YY acknowledge funding from the Chinese National Science Foundation [Grant No.11504110], 111 Project [Grant No.B12024] and Large Instruments Open Foundation of ECNU.

Appendix A. Supplementary data

Supplementary data related to this article can be found at https://doi.org/10.1016/j.actamat.2017.10.018.

References

[1] P.G. de Gennes, Wetting: statics and dynamics, Rev. Mod. Phys. 57 (1985) 827–863, https://doi.org/10.1103/RevModPhys.57.827.
[2] D. Bonn, J. Eggers, J. Indekeu, J. Meunier, E. Rolley, Wetting and spreading, Rev. Mod. Phys. 81 (2009) 739–805, https://doi.org/10.1103/RevModPhys.81.739.
[3] M.N. Popescu, G. Oshanin, S. Dietrich, A.-M. Cazabat, Precursor films in wetting phenomena, J. Phys. Condens. Matter 24 (24) (2012), 243102, https://doi.org/10.1088/0953-8984/24/24/243102.
[4] W.D. Kaplan, D. Chatain, P. Wynblatt, W.C. Carter, A review of wetting versus adsorption, complexions, and related phenomena: the rosetta stone of wetting, J. Mater. Sci. 48 (17) (2013) 5681–5717, https://doi.org/10.1007/s10853-013-7462-y.
[5] Dynamics of electro-wetting droplet transport, Sens. Actuators B Chem. 87 (1) (2002) 201–206, https://doi.org/10.1016/S0925-4005(02)00223-X.
[6] A. Hoang, H.P. Kavehpour, Dynamics of nanoscale precursor film near a moving contact line of spreading drops, Phys. Rev. Lett. 106 (2011), 254501, https://doi.org/10.1103/PhysRevLett.106.254501.
[7] S.L. Cormier, J.D. McGraw, T. Salez, E. Raphaël, K. Dalnoki-Veress, Beyond Tanner's law: crossover between spreading regimes of a viscous droplet on an identical film, Phys. Rev. Lett. 109 (2012), 154501, https://doi.org/10.1103/PhysRevLett.109.154501.
[8] L. Chen, C. Li, N.F.A. van der Vegt, G.K. Auernhammer, E. Bonaccurso, Initial electrospreading of aqueous electrolyte drops, Phys. Rev. Lett. 110 (2013), 026103, https://doi.org/10.1103/PhysRevLett.110.026103.
[9] M. Ilton, O. Bäumchen, K. Dalnoki-Veress, Onset of area-dependent dissipation in droplet spreading, Phys. Rev. Lett. 115 (2015), 046103, https://doi.org/10.1103/PhysRevLett.115.046103.
[10] A. Alizadeh Pahlavan, L. Cueto-Felgueroso, G.H. McKinley, R. Juanes, Thin films in partial wetting: internal selection of contact-line dynamics, Phys. Rev. Lett. 115 (2015), 034502, https://doi.org/10.1103/PhysRevLett.115.034502.
[11] J.D. McGrawa, T.S. Chan, S. Maurer, T. Salez, M. Benzaquen, E. Raphael, M. Brinkmann, K. Jacobs, Slip-mediated dewetting of polymer microdroplets, Proc. Natl. Acad. Sci. U. S. A. 113 (2016) 1168–1173, https://doi.org/10.1073/pnas.1513565113.
[12] T.D. Blake, J. De Coninck, Dynamics of wetting and Kramers' theory, Eur. Phys. J. Spec. Top. 197 (1) (2011) 249–264, https://doi.org/10.1140/epjst/e2011-01467-2.
[13] A. Marchand, S. Das, J.H. Snoeijer, B. Andreotti, Contact angles on a soft solid: from Young's law to Neumann's law, Phys. Rev. Lett. 109 (2012), 236101, https://doi.org/10.1103/PhysRevLett.109.236101.
[14] A.P. Hughes, U. Thiele, A.J. Archer, Liquid drops on a surface: using density functional theory to calculate the binding potential and drop profiles and comparing with results from mesoscopic modelling, J. Chem. Phys. 142 (7) (2015), 074702, https://doi.org/10.1063/1.4907732.
[15] A. Badillo, Quantitative phase-field modeling for wetting phenomena, Phys.

Rev. E 91 (2015), 033005, https://doi.org/10.1103/PhysRevE.91.033005.
[16] A. Giacomello, L. Schimmele, S. Dietrich, Wetting hysteresis induced by nanodefects, Proc. Natl. Acad. Sci. 113 (3) (2015) E262–R271, https://doi.org/10.1073/pnas.1513942113.
[17] R.E. Isele-Holder, A.E. Ismail, Requirements for the formation and shape of microscopic precursors in droplet spreading, Langmuir 32 (18) (2016) 4472–4478, https://doi.org/10.1021/acs.langmuir.6b00807.
[18] R.E. Isele-Holder, A.E. Ismail, Classification of precursors in nanoscale droplets, Phys. Rev. E 93 (2016), 043319, https://doi.org/10.1103/PhysRevE.93.043319.
[19] T. Blake, J. Haynes, Kinetics of liquid/liquid displacement, J. Colloid Interface Sci. 30 (3) (1969) 421–423, https://doi.org/10.1016/0021-9797(69)90411-1.
[20] L.H. Tanner, The spreading of silicone oil drops on horizontal surfaces, J. Phys. D Appl. Phys. 12 (9) (1979) 1473, https://doi.org/10.1088/0022-3727/12/9/009.
[21] R. Cox, The dynamics of the spreading of liquids on a solid surface. part 1. viscous flow, J. Fluid Mech. 168 (1986) 169–194, https://doi.org/10.1017/S0022112086000332.
[22] M.J. de Ruijter, J.D. Coninck, T.D. Blake, A. Clarke, A. Rankin, Contact angle relaxation during the spreading of partially wetting drops, Langmuir 13 (26) (1997) 7293–7298, https://doi.org/10.1021/la970825v.
[23] M.J. de Ruijter, T.D. Blake, J.D. Coninck, Dynamic wetting studied by molecular modeling simulations of droplet spreading, Langmuir 15 (22) (1999) 7836–7847, https://doi.org/10.1021/la9901711.
[24] M.J. de Ruijter, J.D. Coninck, G. Oshanin, Droplet spreading: partial wetting regime revisited, Langmuir 15 (6) (1999) 2209–2216, https://doi.org/10.1021/la971301y.
[25] M.J. de Ruijter, M. Charlot, M. Vou, J.D. Coninck, Experimental evidence of several time scales in drop spreading, Langmuir 16 (5) (2000) 2363–2368, https://doi.org/10.1021/la990769t.
[26] J.D. Coninck, M.J. de Ruijter, M. Voue, Dynamics of wetting, Curr. Opin. Colloid Interface Sci. 6 (1) (2001) 49–53, https://doi.org/10.1016/S1359-0294(00)00087-X.
[27] E.B. Webb, G.S. Grest, D.R. Heine, Precursor film controlled wetting of Pb on Cu, Phys. Rev. Lett. 91 (2003), 236102, https://doi.org/10.1103/PhysRevLett.91.236102.
[28] D.R. Heine, G.S. Grest, E.B. Webb, Spreading dynamics of polymer nanodroplets in cylindrical geometries, Phys. Rev. E 70 (2004), 011606, https://doi.org/10.1103/PhysRevE.70.011606.
[29] T.D. Blake, The physics of moving wetting lines, J. Colloid Interface Sci. 299 (1) (2006) 1–13, https://doi.org/10.1016/j.jcis.2006.03.051.
[30] E. Saiz, A.P. Tomsia, N. Rauch, C. Scheu, M. Ruehle, M. Benhassine, D. Seveno, J. de Coninck, S. Lopez-Esteban, Nonreactive spreading at high temperature: molten metals and oxides on molybdenum, Phys. Rev. E 76 (2007), 041602, https://doi.org/10.1103/PhysRevE.76.041602.
[31] M. Benhassine, E. Saiz, A.P. Tomsia, J.D. Coninck, Nonreactive spreading at high-temperature revisited for metal systems via molecular dynamics, Langmuir 25 (19) (2009) 11450–11458, https://doi.org/10.1021/la902958k.
[32] E. Bertrand, T.D. Blake, J.D. Coninck, Influence of solidliquid interactions on dynamic wetting: a molecular dynamics study, J. Phys. Condens. Matter 21 (46) (2009), 464124, https://doi.org/10.1088/0953-8984/21/46/464124.
[33] S. Mechkov, A.M. Cazabat, G. Oshanin, Post-Tanner stages of droplet spreading: the energy balance approach revisited, J. Phys. Condens. Matter 21 (46) (2009), 464131, https://doi.org/10.1088/0953-8984/21/46/464131.
[34] M. Benhassine, E. Saiz, A. Tomsia, J.D. Coninck, Role of substrate commensurability on non-reactive wetting kinetics of liquid metals, Acta Mater. 58 (6) (2010) 2068–2078, https://doi.org/10.1016/j.actamat.2009.11.049.
[35] M. Benhassine, E. Saiz, A. Tomsia, J.D. Coninck, Nonreactive wetting kinetics of binary alloys: a molecular dynamics study, Acta Mater. 59 (3) (2011) 1087–1094, https://doi.org/10.1016/j.actamat.2010.10.039.
[36] A.M. Tahir, G. Amberg, M. Do-Quang, Initial rapid wetting in metallic systems, Acta Mater. 61 (14) (2013) 5375–5386, https://doi.org/10.1016/j.actamat.2013.05.026.
[37] J. Warren, W. Boettinger, A. Roosen, Modeling reactive wetting, Acta Mater. 46 (9) (1998) 3247–3264, https://doi.org/10.1016/S1359-6454(97)00487-4.
[38] E. Saiz, R. Cannon, A. Tomsia, Reactive spreading: adsorption, ridging and compound formation, Acta Mater. 48 (1819) (2000) 4449–4462, https://doi.org/10.1016/S1359-6454(00)00231-7.
[39] E. Saiz, A. Tomsia, Atomic dynamics and marangoni films during liquid-metal spreading, Nat. Mater 3 (2004) 903–909, https://doi.org/10.1038/nmat1252.
[40] E.B. W III, G.S. Grest, D.R. Heine, J. Hoyt, Dissolutive wetting of Ag on Cu: a molecular dynamics simulation study, Acta Mater. 53 (11) (2005) 3163–3177, https://doi.org/10.1016/j.actamat.2005.03.021.
[41] W. Villanueva, K. Grönhagen, G. Amberg, J. Ågren, Multicomponent and multiphase modeling and simulation of reactive wetting, Phys. Rev. E 77 (2008), 056313, https://doi.org/10.1103/PhysRevE.77.056313.
[42] L. Yin, B.T. Murray, S. Su, Y. Sun, Y. Efraim, H. Taitelbaum, T.J. Singler, Reactive wetting in metalmetal systems, J. Phys. Condens. Matter 21 (46) (2009), 464130, https://doi.org/10.1088/0953-8984/21/46/464130.
[43] W. Villanueva, W. Boettinger, J. Warren, G. Amberg, Effect of phase change and solute diffusion on spreading on a dissolving substrate, Acta Mater. 57 (20) (2009) 6022–6036, https://doi.org/10.1016/j.actamat.2009.08.033.
[44] E. Saiz, M. Benhassine, J.D. Coninck, A. Tomsia, Early stages of dissolutive spreading, Scr. Mater. 62 (12) (2010) 934–938, https://doi.org/10.1016/j.scriptamat.2010.02.046.
[45] D. Wheeler, J.A. Warren, W.J. Boettinger, Modeling the early stages of reactive wetting, Phys. Rev. E 82 (2010), 051601, https://doi.org/10.1103/PhysRevE.82.051601.
[46] T.J. Singler, S. Su, L. Yin, B.T. Murray, Modeling and experiments in dissolutive wetting: a review, J. Mater. Sci. 47 (24) (2012) 8261–8274, https://doi.org/10.1007/s10853-012-6622-9.
[47] D.R. Heine, G.S. Grest, E.B. Webb, Surface wetting of liquid nanodroplets: droplet-size effects, Phys. Rev. Lett. 95 (2005), 107801, https://doi.org/10.1103/PhysRevLett.95.107801.
[48] J.P. Palafox-Hernandez, B.B. Laird, M. Asta, Atomistic characterization of the CuPb solid-liquid interface, Acta Mater. 59 (8) (2011) 3137–3144, https://doi.org/10.1016/j.actamat.2011.01.053.
[49] Y. Yang, M. Asta, B.B. Laird, Solid-liquid interfacial premelting, Phys. Rev. Lett. 110 (2013), 096102, https://doi.org/10.1103/PhysRevLett.110.096102.
[50] H. Gabrisch, L. Kjeldgaard, E. Johnson, U. Dahmen, Equilibrium shape and interface roughening of small liquid Pb inclusions in solid Al, Acta Mater. 49 (20) (2001) 4259–4269, https://doi.org/10.1016/S1359-6454(01)00307-X.
[51] A. Landa, P. Wynblatt, D. Siegel, J. Adams, O. Mryasov, X.-Y. Liu, Development of glue-type potentials for the AlPb system: phase diagram calculation, Acta Mater. 48 (8) (2000) 1753–1761, https://doi.org/10.1016/S1359-6454(00)00002-1.
[52] Y. Yang, D.L. Olmsted, M. Asta, B.B. Laird, Atomistic characterization of the chemically heterogeneous AlPb solidliquid interface, Acta Mater. 60 (12) (2012) 4960–4971, https://doi.org/10.1016/j.actamat.2012.05.016.
[53] R. Kikuchi, J.W. Cahn, Grain-boundary melting transition in a two-dimensional lattice-gas model, Phys. Rev. B 21 (1980) 1893–1897, https://doi.org/10.1103/PhysRevB.21.1893.
[54] R. Lipowsky, Critical surface phenomena at first-order bulk transitions, Phys. Rev. Lett. 49 (1982) 1575–1578, https://doi.org/10.1103/PhysRevLett.49.1575.
[55] P. Stoltze, J.K. Nørskov, U. Landman, Disordering and melting of aluminum surfaces, Phys. Rev. Lett. 61 (1988) 440–443, https://doi.org/10.1103/PhysRevLett.61.440.
[56] A. van der Gon, D. Frenkel, J. Frenken, R. Smith, P. Stoltze, Calculation of ion scattering yields from simulated crystal surfaces: theory and application to melting and non-melting Al surfaces, Surf. Sci. 256 (3) (1991) 385–396, https://doi.org/10.1016/0039-6028(91)90881-R.
[57] W. Theis, K. Horn, Surface premelting in Al(110) observed by core-level photoemission, Phys. Rev. B 51 (1995) 7157–7159, https://doi.org/10.1103/PhysRevB.51.7157.
[58] A.M. Molenbroek, J.W.M. Frenken, Anharmonicity but absence of surface melting on Al(001), Phys. Rev. B 50 (1994) 11132–11141, https://doi.org/10.1103/PhysRevB.50.11132.
[59] N. Marzari, D. Vanderbilt, A. De Vita, M.C. Payne, Thermal contraction and disordering of the Al(110) surface, Phys. Rev. Lett. 82 (1999) 3296–3299, https://doi.org/10.1103/PhysRevLett.82.3296.
[60] See Supporting Information at xxx for a detailed description.
[61] S. Plimpton, Fast parallel algorithms for short-range molecular dynamics, J. Comput. Phys. 117 (1) (1995) 1–19, https://doi.org/10.1006/jcph.1995.1039.
[62] T. Werder, J.H. Walther, R.L. Jaffe, T. Halicioglu, P. Koumoutsakos, On the watercarbon interaction for use in molecular dynamics simulations of graphite and carbon nanotubes, J. Phys. Chem. B 107 (6) (2003) 1345–1352, https://doi.org/10.1021/jp0268112.
[63] J.R. Morris, Complete mapping of the anisotropic free energy of the crystal-melt interface in Al, Phys. Rev. B 66 (2002), 144104, https://doi.org/10.1103/PhysRevB.66.144104.
[64] R.W. Style, E.R. Dufresne, Static wetting on deformable substrates, from liquids to soft solids, Soft Matter 8 (2012) 7177–7184, https://doi.org/10.1039/C2SM25540E.
[65] R.D. Schulman, K. Dalnoki-Veress, Liquid droplets on a highly deformable membrane, Phys. Rev. Lett. 115 (2015), 206101, https://doi.org/10.1103/PhysRevLett.115.206101.
[66] Y. Yang, B.B. Laird, Thermodynamics and intrinsic structure of the alpb liquidliquid interface: a molecular dynamics simulation study, J. Phys. Chem. B 118 (28) (2014) 8373–8380, https://doi.org/10.1021/jp5019313.
[67] M. Gandman, Y. Kauffmann, C.T. Koch, W.D. Kaplan, Direct quantification of ordering at a solid-liquid interface using aberration corrected transmission electron microscopy, Phys. Rev. Lett. 110 (2013), 086106, https://doi.org/10.1103/PhysRevLett.110.086106.
[68] C. Ophus, J. Ciston, J. Pierce, T.R. Harvey, J. Chess, B.J. McMorran, C. Czarnik, H.H. Rose, P. Ercius, Efficient linear phase contrast in scanning transmission electron microscopy with matched illumination and detector interferometry, Nat. Commun. 7 (2016) 10719, https://doi.org/10.1038/ncomms10719.

Supplemental Information for "Droplet Spreading on a Surface Exhibiting Solid-Liquid Interfacial Premelting"

Yang Yang[1] and Brian B. Laird[*2,3]

[1] *State Key Laboratory of Precision Spectroscopy and Physics Department, School of Physical and Material Science, East China Normal University, Shanghai 200062, China*

[2] *Department of Chemistry, University of Kansas, Lawrence, Kansas 66045, United States*

[3] *Freiburg Institute for Advanced Studies, Albertstraße 19, 79104 Freiburg, Germany*

[*] Author to whom correspondence should be addressed

Table of Contents

SECTION S1: SUPPORTING MOVIE FILES

Movie 1: Animation (side view) of the spreading of Pb droplet on Al(111) surface coupled with the premelting transition at 922.38K. The Al atoms are color coded as crystalline (blue) or liquid-like (green) according the the value of the order parameter. The liquid Pb atoms are shown in red. The movie include 6000 successive frames corresponding to a total MD simulation length of 6.0 ns.

Movie 2: Animation (top view) of the upper two surface layers of Al for the droplet-spreading snapshots shown in Movie 1. The Pb atoms not shown. The Al atoms are color coded as crystalline (blue) or liquid-like (green) according the the value of the order parameter. The movie include 6000 successive frames corresponding to a total MD simulation length of 6.0 ns.

SECTION S2. MD SIMULATION OF ALUMINUM CRYSTALS WITH FREE SURFACES

Periodic boundary conditions (PBC) were applied only in the x and y directions, rather than in z, which was defined as the direction normal to the crystal surface, i.e., Al(100), Al(110) and Al(111). The simulation box dimensions ($L_x \times L_y \times L_z$) were approximately 80 Å×80 Å×4 00Å, containing approximately 47000 particles. The distance between the two free surfaces was approximately 0.25 $\times L_z$, to ensure the two free surfaces do not interact. The temperature in all MD simulations was controlled using a Nosé-Hoover thermostat with a thermostat relaxation time of 0.1 ps, and a time step of 1.0 fs. Fcc Al crystals with two free surfaces were prepared, using the equilibrium lattice constant determined for the simulation temperature and pressure. The solid-vapor systems were then equilibrated using an NVT ensemble at several temperatures ranging from $T = 912K$ to $T = 922.38K$. For each temperature, the system was equilibrated for about 10 ns to ensure the total energy, surface density and stresses relaxed to their equilibrium values. In addition, to avoid any Brownian motion of the Al crystal, we subtracted the linear momentum for the innermost layers of the Al crystals during the NVT simulations.

Among the three free surface orientations studied, only Al(110) was seen to undergo a surface premelting transition, which was validated by the fact that the solid surface was covered with a relatively thick (*e.g.*, about 2nm) liquid-like film at temperatures approaching the melting point of Al ($T_{\mathrm{m}}^{\mathrm{Al}}$). However, premelting was not observed for the Al(100) and Al(111) free surfaces in all simulations and for all temperatures studied up to the melting point of Al. Snapshots of equilibrium Al(100), Al(110), Al(111) surfaces at $T = 922.38K$ are shown in Figs. S1, S2 and S3.

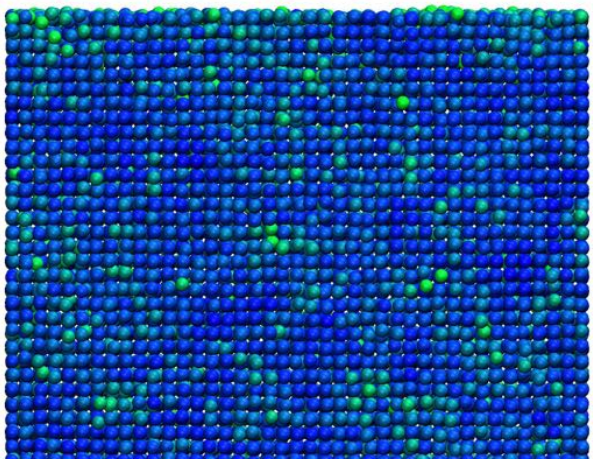

Fig. S1 . Equilibrium MD snapshots of the non-premelted Al(100) surface at 922.38 K. The atom coordinates are projected onto the plane of the page. The Al atoms are color coded as crystalline (blue) or liquid-like (green) according the value of the order parameter.

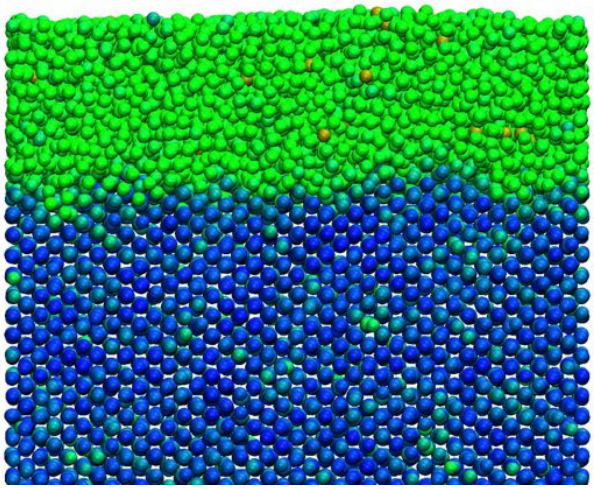

Fig. S2 . Equilibrium MD snapshots of the premelted Al(110) surface at 922.38 K. The atom coordinates are projected onto the plane of the page. The Al atoms are color coded as crystalline (blue) or liquid-like (green) according the value of the order parameter.

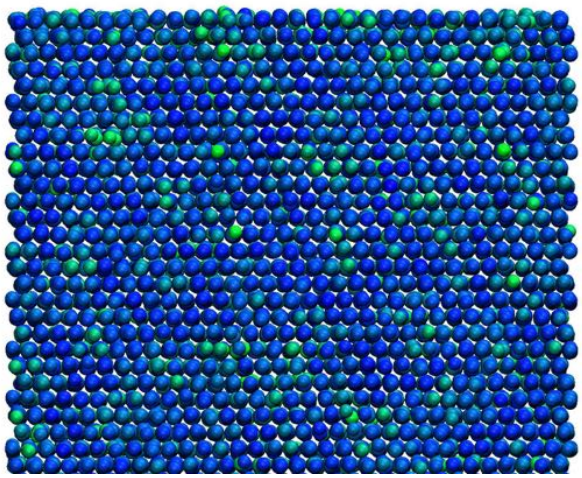

Fig. S3 . Equilibrium MD snapshots of the non-premelted Al(111) surface at 922.38 K. The atom coordinates are projected onto the plane of the page. The Al atoms are color coded as crystalline (blue) or liquid-like (green) according the value of the order parameter.

SECTION S3: EARLY-TIME SPREADING STAGE

Fig. S4 shows the early-time spreading stage (0-0.2 ns) and intermediate kinetic spreading stage (0.2-0.6 ns) on a linear-linear scale, for system A at $T = 922.38$K. The red solid line shows the time evolution averaged over the multiple replica simulations, which are shown individually in grey. The dotted-dash line is the fitting of $R(t)$ to a linear function for the early-time spreading stage, while the dashed line is the fitting to the power law ($R(t) = C_R t^{1/5}$), for the intermediate kinetic spreading stage.

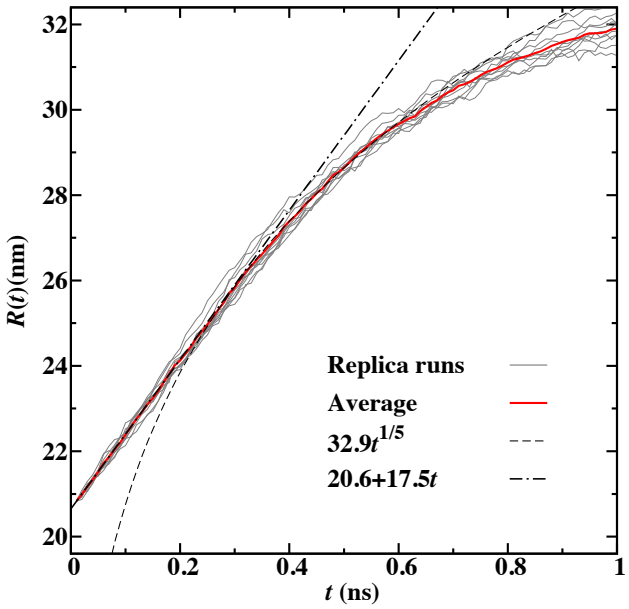

Fig. S4 . Plot of $R(t)$ radius of Pb droplet as a function of time (early-time and intermediate-time stages) for System A at 922.38 K. The red curve shows the radius evolution averaged over the ten replica runs (shown individually in grey). The dashed curve is the fittings to the kinetic model ($R(t) = C_k t^{1/5}$), and the dotted-dash curve is the linear fit of $R(t)$ for early-time spreading stage.

SECTION S4: THERMAL ATOMIC VIBRATIONS OF AL(111) SURFACE

The degree of atomic thermal vibration for the substrate atoms is measured by the atomic mean-square displacement (MSD). The free surface and bulk solid (interior) for the equilibrium Al(111) substrate at several temperatures over a time period of 2 ns. The results are summarized in Table S1.

Spreading on two artificially modified substrates (labelled as V_1 and V_2 in Table 1 in the main text) were studied in this work. In the first (V_1), a harmonic spring force was independently added to each atom in first layer of the Al substrate in order to tether the atom to its ideal lattice position and the value of the force constant is tuned to yield a mean squared displacement for the surface atoms equal to that for the Al(111) free surface atoms at 922.38 K - these values are listed in Table S1. The spring constants used for this simulation are, $K_x = K_y = 0.01 eV/\text{Å}^2$, $K_z = 0.65 eV/\text{Å}^2$. In the simulations, the solid-liquid premelting is artificially suppressed, and long distance interfacial diffusion of Al atoms is limited. In the second modified surface (V_2) , a larger force constant was used to give an artificially harmonically constrained surface at the same temperature (922.38

Tab. S I. The mean-square displacement results for the Al(111) free surfaces.

Al type	T(K)	MSD$_x$(Å^2)	MSD$_y$(Å^2)	MSD$_z$(Å^2)
bulk	922.38	0.085	0.088	0.093
bulk	810	0.064	0.074	0.073
bulk	625	0.049	0.053	0.049
surface	922.38	0.120	0.129	0.169
surface	810	0.088	0.102	0.126
surface	625	0.069	0.068	0.092

K) that has a mean-squared displacement that is 0.25 times that of V_1 ($K_x = K_y = 1.7eV/\text{Å}^2$, $K_z = 4.0eV/\text{Å}^2$).

SECTION S5. $R(t)$ RESULTS FOR INTERMEDIATE TEMPERATURES

A detailed examination of the transition in the spreading kinetics as a function of simulation temperature is shown in Fig.S5. For this figure, in addition to the spreading results for the premelted (922.38 K) and faceted (625 K) substrates presented in the main text, we have added two more simulations at T=835K and T=810K. These additional temperatures are just above and below the roughening transition (T_r=826K) of the Al/Pb solid-liquid interface. The two simulations use the same methods for the MD and post-MD analysis as those discussed in the main text. The Al free surfaces for each of these four temperatures are faceted. From 625 K(green) to 810 K(magenta) to 835 K(orange) and 922.38 K(red), the intermediate time regime follows three different types of spreading kinetics, with the change in the power-law exponent from 1/7 to 1/6 to 1/5. At 810K, a temperature just below the roughening transition, the intermediate spreading regime shows a transition from hydrodynamic dissipation behavior to kinetic dissipation at longer times. The change in behavior in the faceted systems from 625 K to 810 K is likely due to the increase in surface vibrations in the Al surface, increasing the interfacial friction. These results indicate that the change in spreading mechanism from hydrodynamic at 625 K (faceted) to the kinetic mechanism seen in the premelted systems above the roughening transition is due primarily to the increase in surface vibration and not strictly a result of premelting.

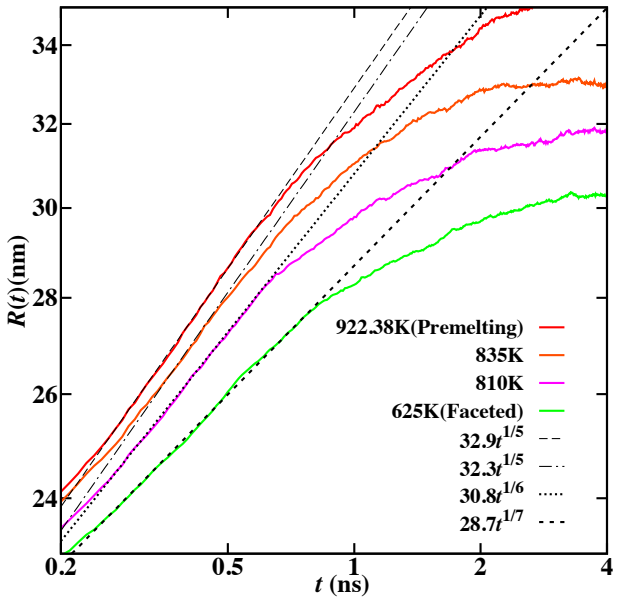

Fig. S5 . Log-Log plot of $R(t)$ radius of Pb droplet as a function of time for System A at four different temperatures. Two temperatures (810K and 835K) are not presented in the main text. The dashed and dotted lines represent power-law fits according to theoretical predictions.